

# Modular tunable coupler for superconducting circuits

Daniel L. Campbell,<sup>1,\*</sup> Archana Kamal,<sup>2</sup> Leonardo Ranzani,<sup>3</sup> Michael Senatore,<sup>1,4</sup> and Matthew LaHaye<sup>1,†</sup>

<sup>1</sup>*Air Force Research Laboratory, Information Directorate, Rome NY 13441 USA*

<sup>2</sup>*Department of Physics and Applied Physics, University of Massachusetts, Lowell, MA 01854 USA*

<sup>3</sup>*Raytheon BBN Technologies, Cambridge MA 02138, USA*

<sup>4</sup>*Department of Physics, Syracuse University, Syracuse NY 13244-1130 USA*

(Dated: July 15, 2022)

The development of modular and versatile quantum interconnect hardware is a key next step in the scaling of quantum information platforms to larger size and greater functionality. For superconducting quantum systems, fast and well-controlled tunable circuit couplers will be paramount for achieving high fidelity and resource efficient connectivity, whether for performing two-qubit gate operations, encoding or decoding a quantum data bus, or interfacing across modalities. Here we propose a modular and internally-tunable coupling architecture that can provide fast and robust linear coupling for several superconducting qubit modalities. The coupling mechanism is mediated by flux-controlled interference in a three-junction dcSQUID and is compatible with the high-fidelity implementation of a variety of functionalities, including two-qubit gate operations, parametric coupling, and quantum bus interfacing.

Recently, several demonstrations of noisy intermediate scale quantum *NISQ* processors involving complex systems comprising tens of coupled qubits, have cemented superconducting circuits as a leading platform for large scale quantum processing [1–5]. Further scaling of quantum processors and the development of distributed quantum architectures will likely benefit from reconfigurable qubit connectivity, tunable dispersive readout, bus interfacing, and transducer interconnects. For all these functionalities the use of a standalone circuit interconnect, a coupler, helps to preserve the coherence of the interconnected circuits while enabling rapid, high fidelity entangling operations between them.

Tunable couplers use an external control parameter to turn on and off an effective coupling  $g_{\text{eff}}$ . In superconducting circuits threading flux through a superconducting quantum interference device (SQUID) and applying microwave driving fields are examples of external control parameters. We highlight two broad approaches to tunable coupling: (i) couplers that use current-divider circuit elements [6–8] (a recent well-known example is the *gmon* coupler [6]), and (ii) couplers that interfere direct and virtual interaction pathways [9–14]. For the latter case, mutual inductance or capacitance between two qubits constitutes a direct interaction pathway while interactions mediated by coupler circuitry constitutes a virtual interaction pathway. Between these two coupling approaches, current divider couplers respond more linearly with flux, lending themselves to parametric coupling applications [7, 8, 15]. However, this approach galvanically connects the qubits, potentially introducing extra flux degrees of freedom, noise, and qubit-qubit crosstalk. Couplers using the interference approach can interface with qubits using capacitive (non-galvanic) interactions that are compatible with high coherence, fixed

frequency, transmon qubits in scaled architectures. As a tradeoff, the frequencies of the qubits and the magnitude of their interaction with the coupler determine the decoupling external flux bias  $\Phi_e^{(0)}$  that zeroes the qubit-qubit effective coupling  $g_{\text{eff}} = 0$ ; this necessitates circuit remodeling and optimization each time data qubits or architecture is even slightly modified. In addition, the quantum level structure of an interference coupler makes the realization of parametrically-driven exchange interactions challenging, an increasingly critical functionality explored in several demonstrations [16–18]. Motivated by these considerations several workarounds, which do not involve modulating the transition frequency of the coupler itself, are gaining traction: such as modulation of the data qubit frequency itself in the presence of a fixed coupling [19–22], and techniques that do not use flux driving [23–25].

In this work, we propose a novel coupler design employing two inductively coupled transmon qubits, which combines the advantages of current divider and interference coupling approaches to achieve fast, linear, and low noise tunable coupling. It is compatible with fixed-frequency qubit architectures and can straightforwardly mitigate distortions in the evolution of the state vector that typically accompany parametric driving. The design paradigm works on a simple principle: each qubit capacitively interacts with a different transmon belonging to the coupler, as illustrated in Figs. 1a-b. These two coupler transmons in turn hybridize with an interaction that can be flux-tuned from negative to positive values. The qubits thus virtually interact via simultaneous coupling to the same hybridized states. Moreover, this net virtual interaction between the qubits can be turned off by flux-tuning the coupler transmon interaction and hybridization to zero. Crucially, the junction and capacitor parameters of the coupler set the functional dependence of the flux-tuning almost exclusively, making the decoupling flux bias  $\Phi_e^{(0)}$  depend only weakly on the transition

\* Daniel.Campbell.22@us.af.mil

† Matthew.LaHaye@us.af.mil

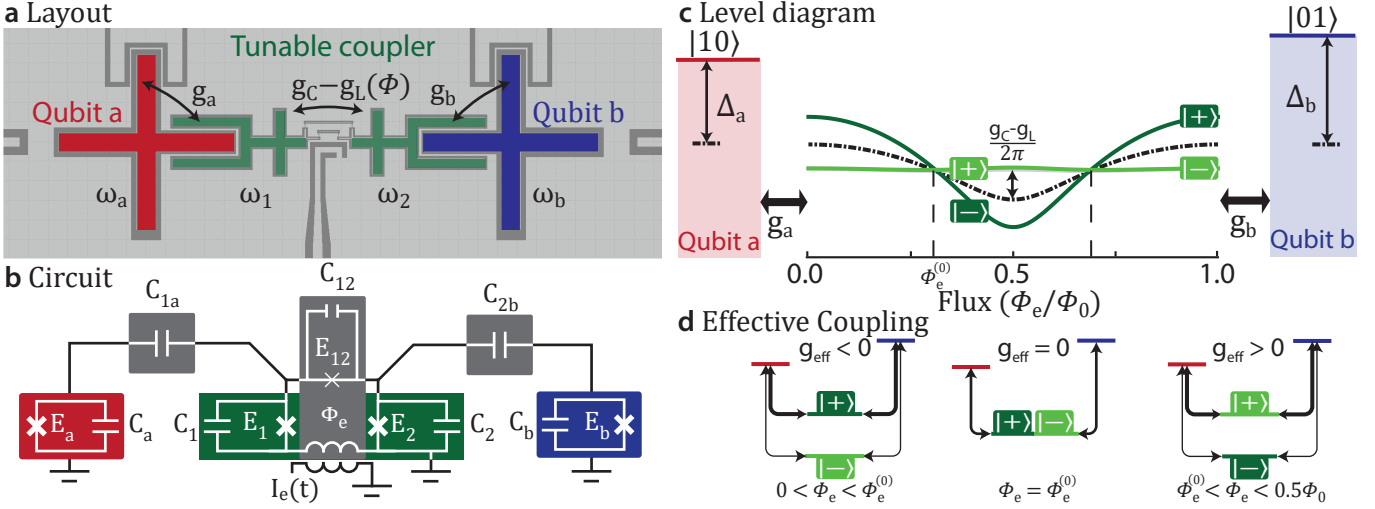


FIG. 1. **a)** Prospective device layout. The coupler consists of a pair of transmon circuits (green) coupled by variably strong capacitance  $g_C$  and strong flux tunable inductance  $g_L(\Phi)$ . Each coupler transmon capacitively couples, in turn, to separate qubits (red and blue).  $\{\omega_a, \omega_1, \omega_2, \omega_b\}/2\pi$  label transmon plasma frequencies in order of appearance, left to right. **b)** The equivalent circuit representation used for the analysis in this work [appendix A]. **c)** A flux-controlled interaction  $g_C - g_L$  turns on a hybridization between the coupler transmons. Solid lines represent hybridized coupler eigenenergies  $\omega_{\pm}$ : the dark and light green lines show  $\omega_{\pm}$  for capacitive coupling  $g_C/2\pi = 0$  MHz and 123 MHz, respectively. Average coupler energy,  $\bar{\omega} = (\omega_1 + \omega_2)/2$ , is represented with the dashed black line. The detuning of each qubit from the average energy is denoted with the detuning  $\Delta_j = \omega_j - \bar{\omega}$  for  $j \in \{a, b\}$ . **d)** Different coupling configurations realized for three distinct flux biases. For simplicity of presentation, we have assumed  $\omega_1 = \omega_2$  (i.e.  $\delta = 0$ ) in (c) and (d), for which the magnitude of the interaction between coupler transmons can be directly read off from the splitting between the  $|+\rangle$  and  $|-\rangle$  eigenstates.

frequencies of the data qubits or qubit-coupler interaction strength (if at all). As a consequence, this *hybridization style* coupler works in a large variety of use cases with little redesign, a desirable feature of modular design.

The proposed coupler circuit consists of two superconducting transmon qubits [26] sharing a common ground. The Josephson and charging energies for each transmon are denoted by  $E_{1,2}$  and  $E_{C_{1,2}}$ , respectively. A relatively high inductance junction  $E_{12} \sim 0.1 \times E_{1,2}$  connects the two transmons, forming a three junction SQUID, see Fig. 1b. A local bias line with an externally sourced current threads a tunable magnetic field through the SQUID, which tunes the inductive interaction between the transmons,

$$g_L = \frac{4E'_{12}\sqrt{E_{C1}E_{C2}}}{\hbar^2\sqrt{\omega_1\omega_2}}, \quad (1)$$

where  $E'_{12} \sim E_{12} \cos(\Phi_e/\phi_0)$  is the external flux-dependent Josephson energy of the center junction [appendix A]. The plasma frequencies,  $\omega_j = (8(E'_j + E'_{12})E_{Cj})^{1/2}$ ,  $j \in \{1, 2\}$ , also tune modestly with flux through flux-dependence of both  $E'_{12}$  and  $E'_j \sim E_j - E_{12}^2 \sin^2(\Phi_e/\phi_0)/2E_j$ . In contrast, the capacitive interaction between the transmons,

$$g_C \approx \frac{C_{12}\sqrt{\omega_1\omega_2}}{2\sqrt{(C_1 + C_{12})(C_2 + C_{12})}}, \quad (2)$$

remains relatively constant as a function of flux. These inductive and capacitive contributions compete to define

the net exchange interaction  $g_C - g_L(\Phi_e)$ , as shown in Fig. 1c [also see Eq. (A6)].

To model and simulate this coupling approach, we consider a chain of four transmon circuits. The outer transmons operate as data qubits with plasma frequencies  $\{\omega_a, \omega_b\}$ , while the inner transmons comprise the coupler with plasma frequencies  $\{\omega_1, \omega_2\}$ . Each qubit capacitively couples to a *different* coupler transmon, with strength  $g_a$  and  $g_b$  respectively. The effective coupling between the data qubits may then be understood as a competition between virtual interactions mediated through the  $|+\rangle$  and  $|-\rangle$  coupler eigenstates, as shown in Fig. 1(d). This allows tuning  $g_{\text{eff}}$  from positive to negative values as a nearly linear function of  $g_C - g_L(\Phi_e)$ , and guarantees the existence of an external flux  $\Phi_e^{(0)}$  such that  $g_{\text{eff}} = 0$ . The coupler transmon anharmonicity contributes perturbatively to  $g_{\text{eff}}$  and  $\Phi_e^{(0)}$ , therefore in the analytical treatment we can treat each transmon as a harmonic oscillator. The resultant Hamiltonian of the full circuit can then be simplified as [see appendix A],

$$H/\hbar = \sum_{j=a,b,1,2} \omega_j a_j^\dagger a_j + (g_C - g_L(\Phi_e))(a_1^\dagger a_2 + a_1 a_2^\dagger) + g_a(a_a^\dagger a_1 + a_a a_1^\dagger) + g_b(a_b^\dagger a_2 + a_b a_2^\dagger), \quad (3)$$

where  $a_j^\dagger$  and  $a_j$  are the raising and lowering operators, while the index  $j$  identifies the respective qubit  $j = \{a, b\}$  or coupler  $j = \{1, 2\}$  transmon modes.

To compute  $g_{\text{eff}}$  we first diagonalize the coupler part of

the circuit, yielding  $\omega_{\pm} = \bar{\omega} \pm (\delta^2 + (g_C - g_L)^2)^{1/2}$  where  $2\bar{\omega} = \omega_1 + \omega_2$  and  $2\delta = \omega_1 - \omega_2$  are the coupler transmon sum and difference plasma frequencies, respectively. Since  $\{\omega_1, \omega_2\}$  move together with flux, the common-mode frequency  $\bar{\omega}$  also tunes with flux, whereas  $\delta$  may tune only weakly, if at all. With  $\delta = 0$ , the modulation of both  $g_L$  and  $\bar{\omega}$  are nearly equal so that one of the two coupler eigenmode plasma frequencies tunes only weakly with flux, as shown in Fig. 1c. In the other regime, when  $\delta \gg |g_C - g_L|$ , both coupler eigenmode plasma frequencies modulate similarly with flux, driven by flux tuning of  $\bar{\omega}$ .

We now consider the data qubit interaction with the coupler eigenmodes. To gain insight into the nature of the coupler operation, we will treat this under the dispersive approximation, i.e.  $g_j/|\omega_j - \omega_{\pm}| < 0.1$ , where approximate analytical expression can be derived. To this end, the first step involves perturbatively decoupling the coupler eigenmodes from the qubit modes using Schrieffer-Wolff transformation of the form  $U_{SW} = \exp\left[\sum_{\pm} \sum_{j=a,b} \frac{g_j}{\omega_j - \omega_{\pm}} (\sigma_j^+ \sigma_{\pm}^- - \sigma_j^- \sigma_{\pm}^+)\right]$ . Retaining terms to second order in  $g_j/(\omega_j - \omega_{\pm})$ , leads to the following effective two-qubit Hamiltonian,

$$\tilde{H}/\hbar \approx \sum_{j=a,b} (\omega_j + \omega_{ac}^j) a_j^\dagger a_j + g_{\text{eff}} (\sigma_a^+ \sigma_b^- + \sigma_a^- \sigma_b^+), \quad (4)$$

with the effective qubit-qubit coupling and dispersive shifts on the qubits given by [see appendix B],

$$g_{\text{eff}} \approx \sum_{j=a,b} \frac{g_a g_b (g_C - g_L)}{2\Delta_j^2 - 2\delta^2 - 2(g_C - g_L)^2}, \quad (5)$$

$$\omega_{ac}^a \approx g_a^2 \left[ \frac{\omega_a - \omega_1}{2\Delta_a^2 - 2\delta^2 - 2(g_C - g_L)^2} \right],$$

$$\omega_{ac}^b \approx g_b^2 \left[ \frac{\omega_b - \omega_2}{2\Delta_b^2 - 2\delta^2 - 2(g_C - g_L)^2} \right]. \quad (6)$$

The flux dependence of  $\bar{\omega}$ , and therefore  $\Delta_j = \omega_j - \bar{\omega}$ , accounts for the non-sinusoidal tuning with flux shown in Fig. 2. Operating in the regimes where  $|\omega_a - \omega_1|, |\omega_b - \omega_2| \gg |g_C - g_L|$  and to a lesser extent when  $\delta \gg |g_C - g_L|$  results in more sinusoidal tuning. For the parameters used in figures of this paper, change in  $\omega_{ac}^j$  with flux is less than/equal to  $g_{\text{eff}}$ .

The externally applied flux ( $\Phi_e$ ) preferentially drops across the junction  $E_{12}$  which has the highest impedance ( $E_{12} \ll E_1, E_2$ ):  $E_{12}$  therefore sets coupler hybridization via  $g_L(\Phi_e)$ . The shunt junctions  $E_1$  and  $E_2$  protect the coupler hybridization from charge noise and interaction with qubits or other external circuitry. As a consequence, the decoupling flux bias,  $\Phi_e^{(0)}$  s.t.  $g_C - g_L(\Phi_e^{(0)}) \propto g_{\text{eff}}(\Phi_e^{(0)}) = 0$ , is *internally defined* by the choice of coupler junction parameters. Figure 2 shows  $g_{\text{eff}}$  for two choices of coupler transmon transitions, above (orange) or below the qubit (blue) transitions. These simulations also show the insensitivity of  $\Phi_e^{(0)}$  to a simulated 6% fabrication variability in all the junction parameters

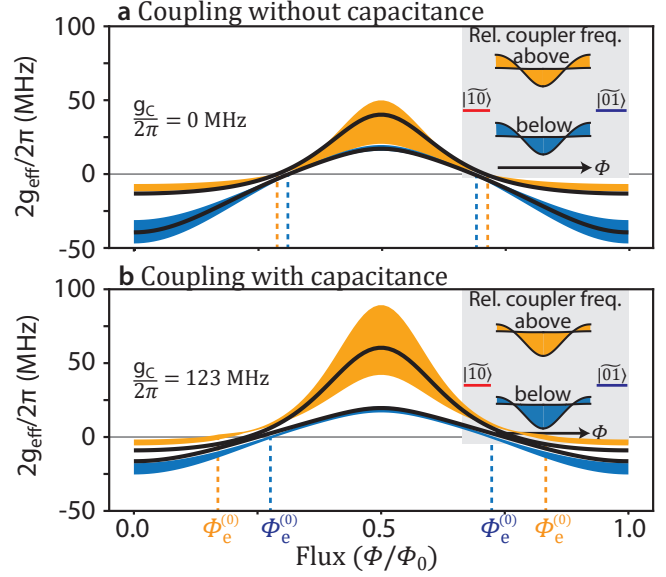


FIG. 2. The  $g_{\text{eff}}$  between degenerate qubits, mediated by the coupler as a function of flux, changes if the coupler transitions are set above versus below the qubit transitions, all else being equal. The shading indicates the effect of 6% variation on all the coupler junctions, obtained using numerical simulation. A comparison of panel (a) versus panel (b) shows that adding capacitance shifts  $g_{\text{eff}}$  to more positive values. For each scenario, the approximate analytic  $g_{\text{eff}}$  is plotted in black [Eq. (5)]. At  $\Phi_e^{(0)}$ , the coupling parameters are given by  $g/2\pi = 0.3$  GHz,  $|\Delta|/2\pi = 1.1$  GHz,  $\delta = 0$ , and the qubit plasma frequencies are  $\omega/2\pi = 4.5$  GHz. The average junction parameters for (a) are  $E_{12}/h = 1.68$  GHz and  $E_1/h, E_2/h = 8.5$  GHz, whereas for (b) they are  $E_{12}/h = 2.7$  GHz and  $E_1/h, E_2/h = 21.7$  GHz. For all calculations, we chose  $E_{12}/h$  to set the maximum inductive coupling to  $g_L/2\pi = 0.35$  GHz.

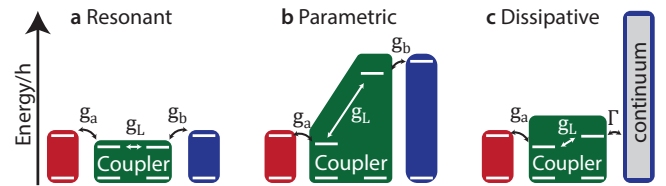


FIG. 3. Quantum state and coupling primitives for resonant, parametric, and dissipative use cases. **a)** A static coupling between nearly resonant qubits may be turned on with a static  $g_L$ . **b)** Parametric coupling between circuit elements with very different transition frequencies may be accomplished by modulating  $g_L$  at the frequency difference. The hybridization of coupler transmons modulates even when its transmon plasma frequencies differ. Coupling magnitude scales inversely with the relative detuning of each coupler transmon from its qubit. **c)** Purcell decay of a qubit through the coupler is turned off when  $g_L = 0$ . This functionality allows waveform shaping of qubit emission into a waveguide.

(shading). Increasing  $g_C$  shifts  $\Phi_e^{(0)}$  further away from  $\Phi_e/\Phi_0 = 0.5$  as shown in Fig. 2b.

The independence of  $\Phi_e^{(0)}$  from qubit plasma frequency

allows for straightforward implementation of degenerate coupling strategies. As an example, consider two qubits, each dispersively coupled to a separate coupler transmon, as shown in Figs. 3a-b. To implement a controlled-Z operation, data qubit b is initialized at a frequency  $\omega_b$  that is 500 MHz higher than  $\omega_a$ ; having some frequency detuning between the qubits helps to mitigate single-qubit microwave crosstalk. Meanwhile, the coupler flux bias is set to  $\Phi_e = \Phi_e^{(0)}$ . Next, by tuning the frequency of either qubit, the state  $|2000\rangle$  is swept into degeneracy with  $|1001\rangle$  (Fig. 3a), where the kets label transmon modes in Fig. 1b from left to right. When the states approach degeneracy,  $\Phi_e$  is ramped away from  $\Phi_e^{(0)}$ , turning on a static coupling. The system then evolves for the requisite dwell time at the resulting avoided level crossing. Subsequently, the inverse of the previous flux ramps is implemented to complete the controlled-Z operation [6, 9, 10, 12, 13]. Unlike interference couplers [9],  $\Phi_e^{(0)}$  remains a constant throughout the procedure, enhancing ease of use.

In a similar manner, it is also possible to implement iSWAP operations via standard approaches [27] utilizing the SQUID coupler. It should be noted, though, that even for evolution under the effective Hamiltonian in Eq. (4) – as is the case for this coupler – turning on  $g_{\text{eff}}$  to perform iSWAP between  $|1000\rangle$  and  $|0001\rangle$  likewise turns on parasitic  $\sigma_z\sigma_z$  phase evolution from interactions in the second excitation manifold  $|0002\rangle \leftrightarrow |1001\rangle$ , which must be separately cancelled [10, 28, 29].

The coupler has some similarities with a capacitively shunted flux (CSFQ) qubit [30]. Like the CSFQ, the anharmonicity of the coupler eigenstates may change as  $\Phi_e$  is swept from zero flux to  $0.5\Phi_0$ . In the  $E_{12} \ll E_1, E_2$  regime, the anharmonicity of the symmetric eigenstate transition of two strongly hybridized transmons  $\omega_1 \simeq \omega_2$  changes from weakly negative (transmon regime) to near zero. In Fig. 1c, the eigenenergy of the symmetric eigenstate can be seen to vary with  $\Phi_e$ , while the small negative anharmonicity of the antisymmetric eigenstate remains constant with  $\Phi_e$ . Unlike interference based couplers where effective  $\sigma_x\sigma_x$  and  $\sigma_z\sigma_z$  interactions cancel at different values of  $\Phi_e$ , partly due to the coupler's anharmonicity [10], a hybridization-based coupler such as the one proposed here can hence eliminate both  $\sigma_x\sigma_x$  and  $\sigma_z\sigma_z$  interactions at  $\Phi_e = \Phi_e^{(0)}$ .

We now discuss how the proposed design can be employed to implement time-dependent parametric coupling. To this end, a parametric modulation of external flux  $\Phi_e = A \sin(\omega_d t) + \Phi_e^{(0)}$  can mediate Rabi-like exchange interactions with rate  $g_{\text{eff}}^p$  between fixed-frequency qubits (or between other circuit elements) by tuning  $\omega_d$  at resonance with the difference of relevant transition frequencies (Fig. 3b). The magnitude of resultant parametric coupling  $g_{\text{eff}}^p$  may be understood in a rotating frame, obtained via the transformation  $(a_a^p, a_1^p, a_b^p, a_2^p) = (a_a, a_1, a_b e^{i\omega_d t}, a_2 e^{i\omega_d t})$ , where qubits  $a$  and  $b$  are rendered degenerate by the parametric driving [Fig. 4(a)].

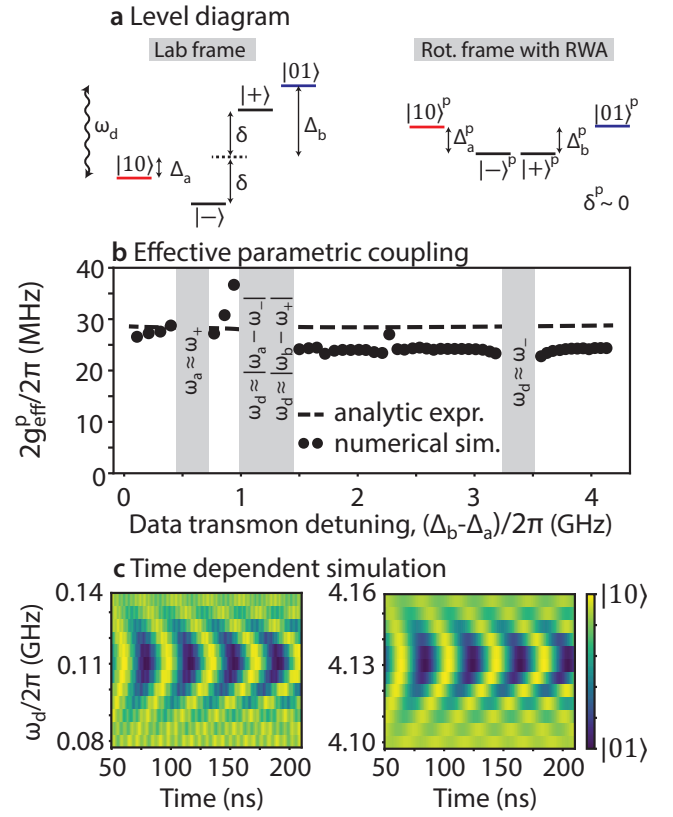


FIG. 4. **a)** Level diagram for parametric coupling defined in reference frames corresponding to the lab (left) and one rotating (right) with the parametric driving field at  $\omega_d$ . We define a new primed coordinate system in the rotating frame. **b)** Sweeping the detuning between the qubit and coupler transmons in lockstep, so that the relative detuning between each qubit and its nearest neighbor coupler transmon remains constant  $\sim 1$  GHz, we find that  $g_{\text{eff}}^p$  also remains constant. This picture breaks down in the shaded regions where accidental degeneracies arise between the qubit and coupler transitions. **c)** Time domain simulations as a function of parametric driving frequency  $\omega_d/2\pi$  and time at qubit-qubit detunings  $(\omega_b - \omega_a)/2\pi$  equal to 0.11 GHz and 4.13 GHz for the (left) and (right) plots, respectively. The drive amplitude increases to its maximum value over 50 ns (not shown).

Neglecting the fast rotating terms, the resulting stationary Hamiltonian is manifestly similar to Eq. (3) with effective coupling given by Eq. (5). Substituting  $\Delta_j^p$ ,  $\delta^p$ , obtained from the level diagram in the rotating frame, and  $g_L^p = (2\pi A - (2\pi A)^3/8)g_L(\Phi_e = 0)$  for their lab-frame terms in Eq. (5), we obtain the effective parametric coupling strength as,

$$g_{\text{eff}}^p \approx \sum_{j=a,b} \frac{-g_a g_b g_L^p}{4(\Delta_j^p)^2 - 4(\delta^p)^2 - 2(g_L^p)^2}. \quad (7)$$

While the qubit detuning and pump frequency need to be swept in tandem to maintain resonance  $\omega_d = \omega_b - \omega_a$ , the relative detuning between coupler transmon/qubit can be kept fixed, i.e.  $|\omega_a - \omega_1| \sim |\omega_b - \omega_2|$ . As a consequence,  $\Delta_j^p$  and  $\delta^p$  also remain constant in the rotating frame.

Adjusting  $g_a$ ,  $g_b$ , and  $g_L^p$  to remain constant as other variables change [appendix A],  $g_{\text{eff}}^p$  can be held constant as a function of flux. Under these circumstances numerical simulation confirm a constant  $g_{\text{eff}}^p$ , as shown in Fig. 4b, in qualitative agreement with Eq. (7). While numerical simulations have included terms up to sixth order in the raising and lowering operators [Fig. A 1], the analytical results are derived using a simplified harmonic oscillator model [Eq. (4)] that neglects anharmonicity. When the coupling is turned on, numerical simulations show  $\sqrt{2}$  stronger coupling within the second excitation manifold compared to within the first excitation manifold, consistent with the simplified analytical model. The qualitative agreement between this model and numerical simulation implies that the anharmonicity of the coupler transmons does not play a strong role in setting  $g_{\text{eff}}$  or  $g_{\text{eff}}^p$ .

Another consideration for parametric coupling is the rectification of data qubit frequency due to flux modulation. Specifically,  $\omega_{ac}^j$  of the driven qubits scales inversely with  $1/(\omega_j - \omega_{\pm})$ , which can change nonlinearly with flux; if the parametric drive periodically brings  $\omega_j$  close to  $\omega_{\pm}$ , it can introduce a time-averaged drive amplitude dependence to the Rabi resonance condition that manifests as distortion of the time-domain swap envelope. As shown by the simulations presented in Fig. 4c, such distortion remains negligible if the coupler-induced frequency shifts are less than  $0.1 \times g_{\text{eff}}^p$ . Relative to interference-based couplers, the proposed coupler mitigates the deleterious impact of the nonlinear flux dependence shifts in two ways. First, the coupler eigenenergies tune gently with effective coupling. Second, the freedom to set the detuning and interaction rate  $g_j$  separately for each coupler transmon/qubit pair in fabrication allows the tuning of  $\omega_{ac}^a$  and  $\omega_{ac}^b$  with flux to be balanced. This balancing strategy roughly maximizes  $g_{\text{eff}}^p$  for a fixed magnitude of nonlinearity. The combination of these factors allows straightforward, and relatively fast, pairwise parametric coupling between non-degenerate fixed-frequency qubits, among other applications. The parameters used in Figs. 2 and 4 represent a worst case scenario for second order nonlinearity generation, where  $\delta \sim 0$ . Even so, parametric coupling of qubits with 110 MHz relative detuning showed Rabi-like state evolution, such as that shown in Fig. 4c, persists as  $E_{12}$  increases 10% (1%) for the coupler transitions placed below (above) the qubit transitions.

A parametric drive can also induce unwanted direct energy exchange between various states in the Hilbert space, i.e.  $\omega_d \approx |\omega_j - \omega_{\pm}|$ , that should be avoided through appropriate choice of coupler transitions in fabrication. This is an important consideration for small qubit detuning. For larger qubit detunings, some driving frequencies will excite the coupler  $\omega_d \sim \omega_{\pm}$ . A weak, undesirable, multi-photon exchange interactions will also occur in the second excited manifold  $|1001\rangle \leftrightarrow |0110\rangle$  when  $\bar{\omega} = (\omega_a + \omega_b)/2$ : choosing the level structure as depicted in Figs. 4 and 3a-b avoids this undesirable degeneracy.

The last use case that we consider is fast tunable coupling between a waveguide (or other open quantum

system) and a qubit, as depicted in Fig. 3c. This use case is thematically consistent with previous demonstrations [16, 31]. For this scenario we make the left data qubit and the right coupler transmon degenerate, i.e.  $\omega_a = \omega_2$ , which invalidates the dispersive approximation used in Eq. (4). Instead, the effective tunable coupling is given by  $g_a(g_C - g_L)/2\delta$ , which goes to zero when the flux is set to  $\Phi_e^{(0)}$ . If the degeneracy between the qubit and coupler transmon is broken, the qubit relaxation rate into the waveguide under the dispersive limit is given by  $\Gamma g_a^2 (g_C - g_L)^2 / (\Delta_a^2 - \delta^2 - (g_C - g_L)^2)^2$ , which is typically small. Further, for  $\omega_a \neq \omega_2$ , the use cases described in Figs. 3b-c can be combined to realize strong coupling to a continuum without demanding degeneracy between qubit and coupler transmon transitions.

Our proposed layout (Fig. 1a) uses a grounded coplanar waveguide with impedance  $Z_0 = 50 \Omega$  that is shorted near the three-junction SQuID loop: current in the waveguide induces a controllable flux  $\Phi_e$  via a mutual inductance  $M$  to the loop. The three junction coupler SQuID allows direct exchange coupling between the coupler states and current excitations in the flux bias line. Using the circuit model discussed in appendix C, the resultant uncorrelated relaxation rate of each coupler transmon into the bias line can be approximated as,  $\Gamma_{1,j} \approx 2\hbar M^2 E_{12}^2 \cos^2(\Phi_e/\phi_0) \omega_j^3 / E_j^2 \Phi_0^2 Z_0$  for  $j \in \{1, 2\}$ , which only doubles if  $g_C$  is increased from zero to  $g_C \sim g_L$ : see the expression for  $\xi_j$  and the derivation for  $\Gamma_{1,j}$  in the appendix C. Therefore, couplers with small mutual inductive coupling  $M \leq 10 \text{ pF}$  likely will not need additional low pass filters on their current bias lines. Conveniently,  $\Gamma_1$  also tunes to zero at  $g_L = 0$ : thus, energy relaxation of the coupler into its flux bias line occurs only when  $g_{\text{eff}} \neq 0$  in the  $g_C \ll g_L$  limit.

Coupler qubit relaxation, whatever the mechanism, is a source of Purcell decay for the qubits  $\Gamma_{1,a} = (g_a/\Delta_a)^2 \Gamma_{1,1}$  and  $\Gamma_{1,b} = (g_b/\Delta_b)^2 \Gamma_{1,2}$  where  $\Gamma_{1,j}$  for  $j \in \{a, 1, 2, b\}$  is the relaxation rate of the relevant transmon. Multi-junction transmons with state-of-the-art fabrication have lifetimes  $T_1 > 20 \mu\text{s}$ ; therefore, the coupler transmons impose at worst a  $200 \mu\text{s}$  energy relaxation time on each qubit given a Purcell factor of  $(g_j/\Delta_j)^2 \sim 1/10$ . While the dispersive regime is considered to be  $(g_j/\Delta_j) < 0.1$ , violating the dispersive approximation condition requires renormalization of  $(g_j/\Delta_j)$  and the inclusion of fourth order terms in the Schrieffer-Wolff transformation for quantitative accuracy [32], but this does not lead to significant deviations from Eqs. (5) and (7) for typical operating conditions.

The impact of coupler-induced dephasing on the qubits can be computed from the frequency response of its eigenstates in presence of fluctuations on loop flux of the SQuID. The coupler eigenenergies change by at most  $4g_L$  over the full flux tuning range, with a maximum slope at the idling flux typically set to the decoupling bias  $\Phi_e^{(0)}$ . At the idling flux, the slope is then  $|\partial\omega/\partial\Phi| = 2g_L/\phi_0$ . For typical amplitudes of flux noise spectral density,  $\sqrt{A_{\Phi}} \sim 2.5 \mu\Phi_0/\sqrt{\text{Hz}}$ , the Hahn echo

---

dephasing rate due to  $1/f$  flux noise can be estimated as  $\Gamma_\phi^E = \sqrt{A_\phi \ln(2)} |\partial\omega/\partial\Phi| \sim 50 \times 10^3 \text{ s}^{-1/2}$  [33]. The frequency fluctuations of the qubits due to flux- and critical-current noise of the coupler transmons are filtered by the Purcell factor  $(g_j/\Delta_j)^2$ . Hence for a Purcell factor of 1/10,  $1/f$  flux noise would limit the coherence of coupled qubit modes to  $\sim 200 \mu\text{s}$  at  $\Phi_e^{(0)}$ .

In summary, we have theoretically explored the use of hybridization between two transmons as a mechanism for mediating tunable interactions between fixed-frequency qubits. The proposed design offers low noise, along with linear and easy-to-model qubit-qubit interactions. Crucially, the decoupling condition is defined by a flux bias that nulls the hybridization, making it almost entirely independent of the properties of the data qubit and qubit-coupler interaction. The extra design freedom afforded by having two coupler transmons rather than one also enables implementation of fast, parametric coupling to a fixed mode or continuum. Moreover, the proposed coupler may be attractive as a standalone qubit for its gentle eigenfrequency tuning with flux, weak exchange coupling with its current bias line, and level structure. The last benefit may also enable novel qutrit-based superconducting circuit architectures [34, 35].

#### ACKNOWLEDGMENTS

This material is based upon work supported by the U.S. Department of Energy, Office of Science, under award number DE-SC0019461, and Air Force Office of Scientific Research under grant FA9550-21-1-0151. Any opinions, findings, and conclusions or recommendations expressed in this article are those of the authors and do not necessarily reflect the views of the Air Force Research Laboratory (AFRL).

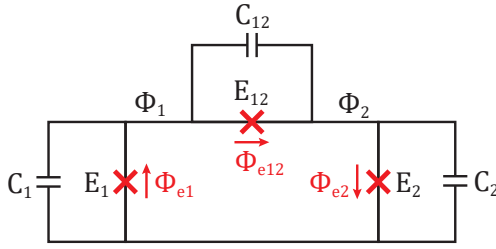


FIG. 5. Coupler circuit comprising two transmons qubits arranged in a flux-tunable loop with a third junction ( $E_{12}, C_{12}$ ).

## Appendix A: Circuit derivation

We write down the Lagrangian using standard circuit parametrization [36–38]

$$\begin{aligned} \mathcal{L} = & \frac{1}{2} C_1 (\dot{\Phi}_1 + \dot{\Phi}_{e1})^2 + \frac{1}{2} C_{12} (\dot{\Phi}_2 - \dot{\Phi}_1 + \dot{\Phi}_{e12})^2 \\ & + \frac{1}{2} C_2 (\dot{\Phi}_2 - \dot{\Phi}_{e2})^2 \\ & + E_1 \cos((\Phi_1 + \Phi_{e1})/\phi_0) + E_2 \cos((\Phi_2 - \Phi_{e2})/\phi_0) \\ & + E_{12} \cos((\Phi_2 - \Phi_1 + \Phi_{e12})/\phi_0), \end{aligned} \quad (\text{A1})$$

where  $\Phi_j(t)$  can be thought of as the node phase or current-like degree of freedom while  $\dot{\Phi}_j(t)$  is the node voltage-like degree of freedom. We use  $\phi_0$  to denote the reduced flux quantum  $\Phi_0/2\pi$ . The loop formed by the three Josephson junctions introduces a constraint which, for our choice of branch sign convention, requires  $\Phi_e = \Phi_{e12} + \Phi_{e1} + \Phi_{e2}$ ; here  $\Phi_e$  is an externally applied flux threaded through the loop, while  $\{\Phi_{e12}, \Phi_{e1}, \Phi_{e2}\}$  denote the branch fluxes across junctions  $\{E_{12}, E_1, E_2\}$  respectively.

Performing the Legendre transformation, we arrive at the Hamiltonian,

$$\begin{aligned} H = & \frac{C_{12}(Q_1 + Q_2)^2}{2C^2} + \frac{C_2 Q_1^2 + C_1 Q_2^2}{2C^2} \\ & + \frac{\dot{\Phi}_{e12}(-Q_1 C_2 C_{12} + Q_2 C_1 C_{12})}{C^2} \\ & + \frac{\dot{\Phi}_{e1}(Q_1(C_1 C_2 + C_1 C_{12}) + Q_2 C_1 C_{12})}{C^2} \\ & - \frac{\dot{\Phi}_{e2}(Q_1 C_1 C_{12} + Q_2(C_1 C_2 + C_1 C_{12}))}{C^2} \\ & - E_1 \cos((\Phi_1 + \Phi_{e1})/\phi_0) - E_2 \cos((\Phi_2 - \Phi_{e2})/\phi_0) \\ & - E_{12} \cos((\Phi_2 - \Phi_1 + \Phi_{e12})/\phi_0), \end{aligned} \quad (\text{A2})$$

where  $C^2 = C_1 C_2 + C_1 C_{12} + C_2 C_{12}$ . Using the loop constraint we may parametrize  $\{\Phi_{e12}, \Phi_{e1}, \Phi_{e2}\}$  in terms

of  $\Phi_e$  such that all  $\dot{\Phi}_e$  terms cancel [38]:

$$\begin{aligned} H = & \frac{C_{12}(Q_1 + Q_2)^2}{2C^2} + \frac{C_2 Q_1^2 + C_1 Q_2^2}{2C^2} \\ & - E_1 \cos \left[ \left( \Phi_1 + \frac{C_{12} C_2}{C^2} \Phi_e \right) / \phi_0 \right] \\ & - E_2 \cos \left[ \left( \Phi_2 - \frac{C_{12} C_1}{C^2} \Phi_e \right) / \phi_0 \right] \\ & - E_{12} \cos \left[ \left( \Phi_2 - \Phi_1 + \frac{C_1 C_2}{C^2} \Phi_e \right) / \phi_0 \right]. \end{aligned} \quad (\text{A3})$$

In this parameterization, we can infer that for typical capacitive coupling,  $C_{12} \leq 0.1\sqrt{C_1 C_2}$ , the participation of  $E_{12}$  with  $\Phi_e$  is greater than 80%. Due to the lack of  $\dot{\Phi}_e$  terms, Eq. (A3) is the simplest construction for charge basis simulations of the Hamiltonian.

Another useful parameterization redistributes  $\Phi_e$  across the junctions to set  $\partial H / \partial \Phi_j = 0$  for  $j = \{1, 2\}$ . This cancels odd order terms in  $\Phi_j$  and thereby enables a straightforward conversion to the harmonic oscillator basis. We assume  $\langle \Phi_j^2 \rangle \ll \Phi_0$  and expand to fourth order in  $\Phi_j$

$$\begin{aligned} H \approx & \frac{C_{12}(Q_1 + Q_2)^2}{2C^2} + \frac{C_2 Q_1^2 + C_1 Q_2^2}{2C^2} \\ & + \frac{\dot{\Phi}_{e12}(-Q_1 C_2 C_{12} + Q_2 C_1 C_{12})}{C^2} \\ & + \frac{E'_{12} \dot{\Phi}_{e12} (Q_1(C_1 C_2 + C_1 C_{12}) + Q_2 C_1 C_{12})}{C^2} \\ & - \frac{E'_{12} \dot{\Phi}_{e12} (Q_1 C_2 C_{12} + Q_2(C_1 C_2 + C_2 C_{12}))}{C^2} \\ & + E'_1 \left( \frac{\Phi_1^2}{2\phi_0^2} - \frac{\Phi_1^4}{24\phi_0^4} \right) \\ & + E'_2 \left( \frac{\Phi_2^2}{2\phi_0^2} - \frac{\Phi_2^4}{24\phi_0^4} \right) \\ & + E'_{12} \left( \frac{(\Phi_2 - \Phi_1)^2}{2\phi_0^2} - \frac{(\Phi_2 - \Phi_1)^4}{24\phi_0^4} \right). \end{aligned} \quad (\text{A4})$$

The external flux is then

$$\begin{aligned} \Phi_e = & \Phi_{e12} + \phi_0 \arcsin((E_{12}/E_1) \sin(\Phi_{e12}/\phi_0)) \\ & + \phi_0 \arcsin((E_{12}/E_2) \sin(\Phi_{e12}/\phi_0)), \end{aligned} \quad (\text{A5})$$

which may be numerically inverted. The junction energies are now flux sensitive:  $E'_{12} = E_{12} \cos(\Phi_{e12}/\phi_0)$  and  $E'_j = \sqrt{E_j^2 - E_{12}^2 \sin^2(\Phi_{e12}/\phi_0)}$ .

### 1. Harmonic oscillator basis

We convert to the Harmonic oscillator basis by substituting  $Q_j = \sqrt{\hbar\omega_j C_{Sj}}/2(a_j + a_j^\dagger)$  and  $\Phi_j = -i\sqrt{\hbar\omega_j L_j/2}(a_j - a_j^\dagger)$  in Eq. (A4). This leads to the following approximate Hamiltonian, with parameters defined in Table I, as

term	value
$C_{S1}$	$\frac{C^2}{C_{12}+C_2}$
$C_{S2}$	$\frac{C^2}{C_{12}+C_1}$
$L_j$	$\frac{\phi_0^2}{E'_{12}+E'_j}$
$E_{Cj}$	$\frac{e^2}{2C_{Sj}}$
$g_C$	$\frac{C_{12}\sqrt{\omega_1\omega_2}}{2\sqrt{(C_1+C_{12})(C_2+C_{12})}}$
$g_L$	$\frac{4E'_{12}\sqrt{E_{C1}E_{C2}}}{\hbar^2\sqrt{\omega_1\omega_2}}$
$\xi_1$	$\frac{(2(E'_1+E'_{12}))^{1/4}[-E'_1(E'_2+E'_{12})C_2C_{12}+E'_2E'_{12}(C_1C_2+C_1C_{12})]}{2E_{C2}^{1/4}E'_1E'_2C^2}$
$\xi_2$	$\frac{(2(E'_2+E'_{12}))^{1/4}[E'_2(E'_1+E'_{12})C_1C_{12}-E'_1E'_{12}(C_1C_2+C_2C_{12})]}{2E_{C2}^{1/4}E'_1E'_2C^2}$
$\omega_j$	$\sqrt{8(E'_j+E'_{12})E_{Cj}}$
$\nu_j^{(4)}$	$\frac{\hbar}{E_{Cj}}\frac{E_{Cj}}{12\hbar}\left(\frac{E_{Cj}}{E'_j+E'_{12}}\right)^{1/2}$
$\nu_j^{(6)}$	$\frac{\sqrt{2}E_{Cj}}{360\hbar}\left(\frac{E_{Cj}}{E'_j+E'_{12}}\right)^{k/4}\left(\frac{E_{C2}}{E'_2+E'_{12}}\right)^{(4-k)/4}$
$\mu_k^{(4)}$	$\binom{4}{k}\frac{(-1)^kE'_{12}}{12\hbar}\left(\frac{E_{C1}}{E'_1+E'_{12}}\right)^{k/4}\left(\frac{E_{C2}}{E'_2+E'_{12}}\right)^{(4-k)/4}$
$\mu_k^{(6)}$	$\binom{6}{k}\frac{(-1)^k\sqrt{2}E'_{12}}{360\hbar}\left(\frac{E_{C1}}{E'_1+E'_{12}}\right)^{k/4}\left(\frac{E_{C2}}{E'_2+E'_{12}}\right)^{(6-k)/4}$

TABLE I. Parameter definitions

$$\begin{aligned}
H/\hbar = & \sum_{j=1}^2 \left[ \omega_j a_j^\dagger a_j - \nu_j^{(4)} (a_j - a_j^\dagger)^4 - \nu_j^{(6)} (a_j - a_j^\dagger)^6 \right] \\
& + g_C (a_1 + a_1^\dagger)(a_2 + a_2^\dagger) + g_L (a_1 - a_1^\dagger)(a_2 - a_2^\dagger) \\
& + \sum_{j=1}^2 \frac{\xi_j \dot{\Phi}_{e12}}{\Phi_0} (a_j + a_j^\dagger) \\
& - \sum_{k=1}^3 \mu_k^{(4)} (a_1 - a_1^\dagger)^k (a_2 - a_2^\dagger)^{(4-k)} \\
& - \sum_{k=1}^3 \mu_k^{(6)} (a_1 - a_1^\dagger)^k (a_2 - a_2^\dagger)^{(6-k)}. \quad (\text{A6})
\end{aligned}$$

The terms fourth order in the raising and lowering operators modify the eigenenergies in the harmonic oscillator basis by several hundred MHz and account for the majority of the anharmonicity. The sixth order terms compensate for a residual few 10s of MHz of discrepancy between the charge basis and harmonic oscillator approaches to simulation. At sixth order in the raising and lowering operators the first and second excitation manifolds of eigenenergies for the two simulation approaches agree to within 1 MHz, shown together in Fig. A 1.

## Appendix B: Analytical derivation

To apply the standard machinery of the Schrieffer-Wolff transformation to decouple the states of the coupler from the computational Hilbert space we must first diagonalize the coupler states. Exact analytic diagonalization at second order in raising and lowering operators (this neglects anharmonicity) may be performed using

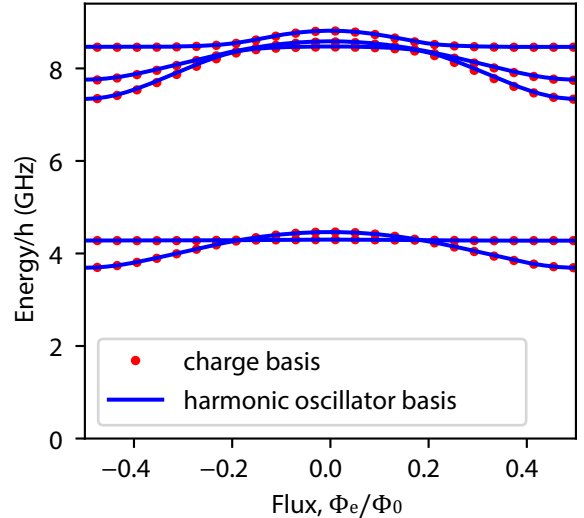


FIG. 6. Comparison of the eigenstates produced by a harmonic oscillator basis simulation (blue) compared to a charge basis simulation. We chose parameters  $E_j = 13$  GHz,  $E_{12} = 1.3$  GHz,  $C_j = 100$  fF, and  $C_{12} = 0$  fF. We simulated 8 levels per qubit for the harmonic oscillator simulation and 14 Cooper pair levels in the charge simulation.

the Bogoliubov transformation,

$$\mathbb{H} = \Psi^\dagger K \Psi, \quad (\text{B1})$$

where  $\Psi^\dagger = (a_1 \ a_1^\dagger \ a_2 \ a_2^\dagger)$  and

$$K = \begin{pmatrix} \omega_1 & 0 & g_C - g_L & g_C + g_L \\ 0 & \omega_1 & g_C + g_L & g_C - g_L \\ g_C - g_L & g_C + g_L & \omega_2 & 0 \\ g_C + g_L & g_C - g_L & 0 & \omega_2 \end{pmatrix}. \quad (\text{B2})$$

The idea is to perform a similarity transformation to diagonalize  $K$  and thereby find a diagonal parametrization of  $\mathbb{H}$ , which is a redundant construction of the conventional Hamiltonian  $H$ .

Interestingly, because  $[\Psi_i^\dagger, \Psi_j] = (-1)^i \delta_{i,j}$ , a similarity transformation is likely to produce a set of transformed operators that no longer obey the bosonic commutation relations. We can fix this by identifying the transformation  $\sigma = (-1)^i \delta_{i,j}$ , applying it to the column vector  $[\Psi_i^\dagger, \sigma \Psi_j] = \sigma \sigma = \delta_{i,j}$ , where the commutation relations are now uniform. The resulting similarity transformation  $T$  takes the form

$$T^\dagger \sigma \sigma K T = T^{-1} \sigma K T = \sigma K' \quad (\text{B3})$$

where  $K'$  is the desired diagonal form of  $K$  and  $\Psi = T \Psi'$ , see Altland and Simons, page 72 [39]. Using this technique, the diagonal form of the coupler operators (neglecting anharmonic terms) can be found by diagonalizing  $\sigma K$ . The corresponding eigenenergies  $\{\omega_\pm, -\omega_\pm\}$

(neglecting anharmonic terms) are given by,

$$\omega_{\pm} = \sqrt{2\bar{\omega}^2 - \omega_1\omega_2 - 4g_Cg_L} \pm 2\eta, \quad (\text{B4})$$

with  $\eta = \sqrt{\delta^2\bar{\omega}^2 + (g_C + g_L)^2\omega_1\omega_2 - 4g_Cg_L\bar{\omega}^2}$ .

### 1. Co-rotating terms

Neglecting terms proportional to  $g_C + g_L$  in Eq. (B2) allows a compact representation of the approximate eigenvectors  $T$ , which we apply to derive an analytic form of the effective coupling as mediated by exchange interactions. The approximate eigenenergies are likewise simplified to

$$\omega_{\pm} = \bar{\omega} \pm \sqrt{\delta^2 + (g_C - g_L)^2}, \quad (\text{B5})$$

where  $\bar{\omega} = (\omega_1 + \omega_2)/2$  and  $\delta = (\omega_1 - \omega_2)/2$ . The corresponding eigenvectors now take the form

$$a_- = -\sqrt{1 - \beta^2}a_1 + \beta a_2, \quad (\text{B6a})$$

$$a_+ = \beta a_1 + \sqrt{1 - \beta^2}a_2, \quad (\text{B6b})$$

where  $\beta = A/\sqrt{(g_C - g_L)^2 + A^2}$ , with  $A = \delta + \sqrt{\delta^2 + (g_C - g_L)^2}$ . If  $\delta = 0$  then the coupler transmons are degenerate and therefore fully hybridized, leading to  $\beta = 1/\sqrt{2}$  as we might expect. Substituting the eigenoperators  $a_{\pm}$  for  $a_{1,2}$  in Eq. (A6) and retaining terms to second order, we obtain

$$H = H_0 + V \quad (\text{B7})$$

with

$$H_0/\hbar = \omega_a a_a^\dagger a_a + \omega_b a_b^\dagger a_b + \omega_- a_-^\dagger a_- + \omega_+ a_+^\dagger a_+, \quad (\text{B8a})$$

$$\begin{aligned} V/\hbar = & -\sqrt{1 - \beta^2}g_a(a_a + a_a^\dagger)(a_- + a_-^\dagger) \\ & + \beta g_b(a_b + a_b^\dagger)(a_- + a_-^\dagger) \\ & + \beta g_a(a_a + a_a^\dagger)(a_+ + a_+^\dagger) \\ & + \sqrt{1 - \beta^2}g_b(a_b + a_b^\dagger)(a_+ + a_+^\dagger). \end{aligned} \quad (\text{B8b})$$

We identify a Schrieffer-Wolff generator  $S$  such that  $[H_0, S] = V$ ,

$$\begin{aligned} S/\hbar = & \frac{-\sqrt{1 - \beta^2}g_a}{\Delta_{a-}}(a_a^\dagger a_- - a_a a_-^\dagger) + \frac{\beta g_b}{\Delta_{b-}}(a_b^\dagger a_- - a_b a_-^\dagger) \\ & + \frac{\beta g_a}{\Delta_{a+}}(a_a^\dagger a_+ - a_a a_+^\dagger) + \frac{\sqrt{1 - \beta^2}g_b}{\Delta_{b+}}(a_b^\dagger a_+ - a_b a_+^\dagger) \\ & + \frac{-\sqrt{1 - \beta^2}g_a}{\Sigma_{a-}}(a_a^\dagger a_-^\dagger - a_a a_-) + \frac{\beta g_b}{\Sigma_{b-}}(a_b^\dagger a_-^\dagger - a_b a_-) \\ & + \frac{\beta g_a}{\Sigma_{a+}}(a_a^\dagger a_+^\dagger - a_a a_+) + \frac{\sqrt{1 - \beta^2}g_b}{\Sigma_{b+}}(a_b^\dagger a_+^\dagger - a_b a_+), \end{aligned} \quad (\text{B9})$$

where  $\Delta_{j\pm} = \omega_j - \omega_{\pm} = \Delta_j \pm \sqrt{\delta^2 + (g_C - g_L)^2}$  and, as defined in the main text,  $\Delta_j = \omega_j - \bar{\omega}$ . Then

$$H' = e^S H e^{-S} = H_0 + [S, V]/2 + \mathcal{O}(V^3) \quad (\text{B10})$$

is the leading order diagonalized Hamiltonian with the pre-factor of the lowest order term  $[S, V]/2$  setting the effective coupling

$$\begin{aligned} g_{\text{eff}} = & \frac{g_a g_b \beta \sqrt{1 - \beta^2}}{2} \left[ \frac{1}{\Delta_{a+}} + \frac{1}{\Delta_{b+}} + \frac{1}{\Sigma_{a+}} + \frac{1}{\Sigma_{b+}} \right. \\ & \left. - \frac{1}{\Delta_{a-}} - \frac{1}{\Delta_{b-}} - \frac{1}{\Sigma_{a-}} - \frac{1}{\Sigma_{b-}} \right]. \end{aligned} \quad (\text{B11})$$

We may further rearrange terms to obtain the equation quoted in the main text

$$g_{\text{eff}} = \sum_{j=a,b} \frac{g_a g_b \left[ g_C - g_L + (g_C + g_L) \frac{\Delta_j}{\bar{\omega}} \right]}{2\Delta_j^2 - 2\delta^2 - 2(g_C - g_L)^2}. \quad (\text{B12})$$

The ac Stark shifts on the data qubits may be calculated similarly

$$\begin{aligned} \omega_a^{\text{ac}} = & \frac{g_a^2}{2} \left[ \frac{\beta^2}{\Delta_{a+}} + \frac{1 - \beta^2}{\Delta_{a-}} - \frac{\beta^2}{\Sigma_{a+}} - \frac{1 - \beta^2}{\Sigma_{a-}} \right] \\ \omega_a^{\text{ac}} = & \frac{g_a^2}{2} \left[ \frac{\omega_a - \omega_1}{\Delta_a^2 - \delta^2 - (g_C - g_L)^2} + \frac{-\omega_a - \omega_1}{\Sigma_a^2 - \delta^2 - (g_C - g_L)^2} \right] \\ \omega_b^{\text{ac}} = & \frac{g_b^2}{2} \left[ \frac{1 - \beta^2}{\Delta_{b+}} + \frac{\beta^2}{\Delta_{b-}} - \frac{1 - \beta^2}{\Sigma_{b+}} - \frac{\beta^2}{\Sigma_{b-}} \right] \\ \omega_b^{\text{ac}} = & \frac{g_b^2}{2} \left[ \frac{\omega_b - \omega_2}{\Delta_b^2 - \delta^2 - (g_C - g_L)^2} + \frac{-\omega_b - \omega_2}{\Sigma_b^2 - \delta^2 - (g_C - g_L)^2} \right]. \end{aligned} \quad (\text{B13})$$

### 2. Counter-rotating terms

Neglecting now the terms proportional to  $g_C - g_L$  in Eq. (B2), we can calculate the approximate eigenenergies,

$$\omega_{\pm} = \pm\delta + \sqrt{\bar{\omega}^2 - (g_C + g_L)^2}, \quad (\text{B14})$$

and the eigenvectors,

$$a_+ = \alpha a_1 - i\sqrt{1 - \alpha^2}a_2^\dagger, \quad (\text{B15a})$$

$$a_- = \alpha a_2 - i\sqrt{1 - \alpha^2}a_1^\dagger, \quad (\text{B15b})$$

with  $\alpha = D/\sqrt{(g_C + g_L)^2 + D^2}$ ,  $D = \bar{\omega} + \sqrt{\bar{\omega}^2 - (g_C + g_L)^2}$ . Note that here we have neglected the direct exchange interaction terms. Substituting the transformed operators for  $a_{1,2}$  in Eq. (A6) leads to the interaction,

$$\begin{aligned} V/\hbar = & i\sqrt{1 - \alpha^2}g_a(a_a + a_a^\dagger)(a_- - a_-^\dagger) \\ & + \alpha g_b(a_b + a_b^\dagger)(a_- + a_-^\dagger) \\ & + \alpha g_a(a_a + a_a^\dagger)(a_+ + a_+^\dagger) \\ & + i\sqrt{1 - \alpha^2}g_b(a_b + a_b^\dagger)(a_+ - a_+^\dagger), \end{aligned} \quad (\text{B16})$$

which can be transformed using the generator,

$$\begin{aligned}
S/\hbar = & \frac{i\sqrt{1-\alpha^2}g_a}{\Delta_{a-}}(a_a^\dagger a_- + a_a a_-^\dagger) + \frac{\alpha g_b}{\Delta_{b-}}(a_b^\dagger a_- - a_b a_-^\dagger) \\
& + \frac{\alpha g_a}{\Delta_{a+}}(a_a^\dagger a_+ - a_a a_+^\dagger) + \frac{i\sqrt{1-\alpha^2}g_b}{\Delta_{b+}}(a_b^\dagger a_+ + a_b a_+^\dagger) \\
& + \frac{i\sqrt{1-\alpha^2}g_a}{\Sigma_{a-}}(-a_a^\dagger a_-^\dagger - a_a a_-) + \frac{\alpha g_b}{\Sigma_{b-}}(a_b^\dagger a_-^\dagger - a_b a_-) \\
& + \frac{\alpha g_a}{\Sigma_{a+}}(a_a^\dagger a_+^\dagger - a_a a_+) + \frac{i\sqrt{1-\alpha^2}g_b}{\Sigma_{b+}}(-a_b^\dagger a_+^\dagger - a_b a_+),
\end{aligned} \tag{B17}$$

to obtain the effective qubit-qubit coupling,

$$H_{\text{eff}} = ig_1(a_a^\dagger + a_a)(a_b - a_b^\dagger) + ig_2(a_b^\dagger + a_b)(a_a - a_a^\dagger) \tag{B18}$$

where

$$g_1 = \frac{\alpha\sqrt{1-\alpha^2}g_a g_b}{2} \left[ \frac{1}{\Delta_{b-}} + \frac{1}{\Delta_{b+}} - \frac{1}{\Sigma_{b-}} - \frac{1}{\Sigma_{b+}} \right], \tag{B19a}$$

$$g_2 = \frac{\alpha\sqrt{1-\alpha^2}g_a g_b}{2} \left[ \frac{1}{\Delta_{a-}} + \frac{1}{\Delta_{a+}} - \frac{1}{\Sigma_{a-}} - \frac{1}{\Sigma_{a+}} \right]. \tag{B19b}$$

## Appendix C: Noise analysis

### 1. Coherence

The Gaussian pure dephasing rate due to  $1/f$  flux noise is  $\Gamma_\phi^E = \sqrt{A_\Phi \ln 2} |\partial\omega/\partial\Phi|$  for Hahn echo measurements. It depends upon the noise amplitude  $\sqrt{A_\Phi}$ , defined at  $\omega/2\pi = 1$  Hz, of the power spectral density  $S(\omega)_\Phi = A_\Phi/|\omega|$  and the slope of the energy dispersion with flux  $\hbar\partial\omega/\partial\Phi$ . Careful engineering gives a noise amplitude  $\sqrt{A_\Phi} \sim 2.5\mu\Phi_0$ .

On the coupler, the peak to peak difference in the frequency dispersion is  $\sim 0.6$  GHz, giving  $\Gamma_\phi^E \approx 2.5\mu\Phi_0\sqrt{\ln(2)}(2\pi)^2 \times 0.3$  GHz/ $\Phi_0 = 1/40$   $\mu$ s. The noise on  $g_{\text{eff}}$  from the flux sensitivity on  $g_L$  is then reduced by a factor  $g_a g_b / (2\Delta_j^2 - 2\delta^2)$ . Similarly, frequency noise on the qubits from the flux sensitivity on  $\bar{\omega}$  is reduced by a factor of  $\sim g_a^2 / (2\Delta_j^2 - 2\delta^2)$ . For  $g_{\text{eff}} = 2\pi \times 60$  MHz, the coupler limits the pure dephasing lifetime to  $T_\phi^E \sim 400$   $\mu$ s.

### 2. Energy relaxation

Energy relaxation of a qubit into its nearest neighbor coupler transmon is approximately given by the Purcell formula. Using the definitions in the main text and sup-

plement the coupler induces relaxation of qubit a

$$\begin{aligned}
\Gamma_{1,a}^{\text{Purcell}} & \approx g_a^2 \left( \frac{\Gamma_{1,+}\beta^2}{\Delta_{a+}^2} + \frac{\Gamma_{1,-}(1-\beta^2)}{\Delta_{a-}^2} \right) \\
& \sim \frac{\Gamma_{1,1}g_a^2}{(\omega_a - \omega_1)^2}.
\end{aligned} \tag{C1}$$

Similarly, for qubit b

$$\begin{aligned}
\Gamma_{1,b}^{\text{Purcell}} & \approx g_b^2 \left( \frac{\Gamma_{1,-}\beta^2}{\Delta_{b-}^2} + \frac{\Gamma_{1,+}(1-\beta^2)}{\Delta_{b+}^2} \right) \\
& \sim \frac{\Gamma_{1,2}g_b^2}{(\omega_b - \omega_2)^2}.
\end{aligned} \tag{C2}$$

The energy relaxation rates for coupler transmons 1 and 2 are given by  $\Gamma_{1,1}$  and  $\Gamma_{1,2}$ , respectively. While these quantities are not true observables of the system since the coupler transmons can be strongly hybridized, we want to emphasize that qubit a is not very sensitive to relaxation channels local to coupler transmon 2, nor is qubit b sensitive to relaxation channels local to coupler transmon 1. In the case of direct measurement of coupler relaxation rates, or if we expect correlated relaxation processes, then  $\Gamma_{1,+}$  and  $\Gamma_{1,-}$  describe the energy relaxation rate of the upper and lower hybridized states, respectively.

Plugging in 20  $\mu$ s as a reasonable lower bound on each coupler transmon's energy relaxation lifetime, the induced  $T_1$  on a neighboring data qubit is 220  $\mu$ s for a  $g/\Delta$  ratio of 0.3.

### 3. Coupling a qubit to an open quantum system

We consider coupling qubit a to a bath as mediated by the tunable coupler. In this scenario a deliberate interaction with the bath induces coupler transmon 2 to relax with rate  $\Gamma_{1,2}$  into the bath.

$$\begin{aligned}
\Gamma_{1,a} & \approx \Gamma_{1,2}g_a^2\beta^2(1-\beta^2) \left( \frac{1}{\Delta_{a+}^2} + \frac{1}{\Delta_{a-}^2} \right) \\
& \approx \frac{\Gamma_{1,2}(g_C - g_L)^2 g_a^2}{(\Delta_a^2 - \delta^2 - (g_C - g_L)^2)^2}
\end{aligned} \tag{C3}$$

We see that the coupler isolates the qubit from dissipation on the next-to-nearest-neighbor coupler transmon to fourth order in  $g_C - g_L$ ,  $g_a/\Delta_a$ . Although  $\Gamma_{1,a}$  turns off at  $g_C - g_L = 0$ , it is difficult to achieve sizeable 'on'  $\Gamma_a$  values using the coupler in dispersive operation. This weak 'on' interaction motivates the alternative approach taken in the main text.

### 4. Energy relaxation into the flux bias line

A critical consideration for choosing an appropriate mutual inductance between the coupler SQuID and its flux bias line is the relaxation rate of the coupler induced

due to this inductive coupling. This relaxation can lead to strong correlations if  $\delta \ll |g_C - g_L|$ . In this circumstance the ‘bright’ state is the one that tunes strongly with flux and will relax, at worst, at the sum of the individual transmon relaxation rates. In the other regime  $\delta \gg |g_C - g_L|$ , the eigenstates  $|\pm\rangle$  are closely approximated by independent transmon eigenstates, such that we can approximately map  $\xi_j \leftrightarrow \xi_{\pm}$  for  $j \in \{1, 2\}$ . Assuming  $\dot{\Phi}_e = M\dot{I}$ , this allows us to write the effective decay rate as,

$$\begin{aligned}\Gamma_{1,\pm}^{fb} &\sim \left(\frac{\xi_{\pm}(\Phi_e)M}{\Phi_0}\right)^2 S_{II}(\omega) \\ &= \frac{2\hbar\xi_{\pm}^2(\Phi_e)M^2\omega_{\pm}^3}{\Phi_0^2Z_0},\end{aligned}\quad (\text{C4})$$

where in the first line we have used the flux participation ratio as prescribed by the third line of Eq. (A6), and in the second line we have assumed that the magnitude of current fluctuations is set by their vacuum expectation value, i.e.  $S_{II}(\omega) = \omega_{\pm}^2 S_{II}(\omega) = 2\hbar\omega_{\pm}^3/Z_0$ .

Given a mutual inductance  $M = 16$  pH, capacitive coupling  $C_{12} \ll C_1, C_2$ , dimensionless coupling constant  $\xi_{\pm}(0) \sim E'_{12}(0)/E'_1(0)$ , or  $E'_{12}(0)/E'_2(0)$ , transition frequency  $\omega_{\pm}/2\pi = 5$  GHz, and bath impedance of 50 Ohms, the equation above leads to an estimated  $\Gamma_{1,\pm}^{fb} \sim 2 \times 10^3$  s<sup>-1</sup>, before additional low pass filtering of the flux bias. We note that these are worst case calculations since  $\xi_{\pm}(\Phi_e) \propto \cos(2\pi\Phi_e/\Phi_0)$ , which at  $\Phi_e^{(0)} \sim 0.25\Phi_0$  causes the dimensionless coupling constant  $\xi(\Phi_e)$  to vanish.

[1] A. Cross, in *APS March Meeting Abstracts*, Vol. 2018 (2018) pp. L58–003.

[2] F. Arute, K. Arya, R. Babbush, D. Bacon, J. C. Bardin, R. Barends, R. Biswas, S. Boixo, F. G. Brandao, D. A. Buell, *et al.*, *Nature* **574**, 505 (2019).

[3] M. Gong, S. Wang, C. Zha, M.-C. Chen, H.-L. Huang, Y. Wu, Q. Zhu, Y. Zhao, S. Li, S. Guo, *et al.*, *Science* **372**, 948 (2021).

[4] G. Q. AI, *Nature* **595**, 383 (2021).

[5] Y. Wu, W.-S. Bao, S. Cao, F. Chen, M.-C. Chen, X. Chen, T.-H. Chung, H. Deng, Y. Du, D. Fan, *et al.*, *Physical Review Letters* **127**, 180501 (2021).

[6] Y. Chen, C. Neill, P. Roushan, N. Leung, M. Fang, R. Barends, J. Kelly, B. Campbell, Z. Chen, B. Chiaro, A. Dunsworth, E. Jeffrey, A. Megrant, J. Y. Mutus, P. J. J. O’Malley, C. M. Quintana, D. Sank, A. Vainsencher, J. Wenner, T. C. White, M. R. Geller, A. N. Cleland, and J. M. Martinis, *Phys. Rev. Lett.* **113**, 220502 (2014), publisher: American Physical Society.

[7] P. Roushan, C. Neill, A. Megrant, Y. Chen, R. Babbush, R. Barends, B. Campbell, Z. Chen, B. Chiaro, A. Dunsworth, and et al., *Nature Physics* **13**, 146–151 (2016).

[8] T. Noh, Z. Xiao, K. Cicak, X. Y. Jin, E. Doucet, J. Teufel, J. Aumentado, L. C. G. Govia, L. Ranzani, A. Kamal, and R. W. Simmonds, Strong parametric dispersive shifts in a statically decoupled multi-qubit cavity qed system (2021), arXiv:2103.09277 [quant-ph].

[9] F. Yan, P. Krantz, Y. Sung, M. Kjaergaard, D. L. Campbell, T. P. Orlando, S. Gustavsson, and W. D. Oliver, *Phys. Rev. Applied* **10**, 054062 (2018), publisher: American Physical Society.

[10] Y. Sung, L. Ding, J. Braumüller, A. Vepsäläinen, B. Kannan, M. Kjaergaard, A. Greene, G. O. Samach, C. McNally, D. Kim, A. Melville, B. M. Niedzielski, M. E. Schwartz, J. L. Yoder, T. P. Orlando, S. Gustavsson, and W. D. Oliver, *Phys. Rev. X* **11**, 021058 (2021).

[11] X. Li, T. Cai, H. Yan, Z. Wang, X. Pan, Y. Ma, W. Cai, J. Han, Z. Hua, X. Han, Y. Wu, H. Zhang, H. Wang, Y. Song, L. Duan, and L. Sun, *Phys. Rev. Applied* **14**, 024070 (2020), publisher: American Physical Society.

[12] M. C. Collodo, J. Herrmann, N. Lacroix, C. K. Andersen, A. Remm, S. Lazar, J.-C. Besse, T. Walter, A. Wallraff, and C. Eichler, arXiv:2005.08863 [quant-ph] (2020), arXiv: 2005.08863.

[13] Y. Xu, J. Chu, J. Yuan, J. Qiu, Y. Zhou, L. Zhang, X. Tan, Y. Yu, S. Liu, J. Li, F. Yan, and D. Yu, arXiv:2006.11860 [quant-ph] (2020), arXiv: 2006.11860.

[14] J. Stehlik, D. M. Zajac, D. L. Underwood, T. Phung, J. Blair, S. Carnevale, D. Klaus, G. A. Keefe, A. Carniol, M. Kumph, and et al., *Physical Review Letters* **127**, 10.1103/physrevlett.127.080505 (2021).

[15] E. Zakka-Bajjani, F. Nguyen, M. Lee, L. R. Vale, R. W. Simmonds, and J. Aumentado, *Nature Physics* **7**, 599–603 (2011).

[16] J.-C. Besse, K. Reuer, M. C. Collodo, A. Wulff, L. Wernli, A. Copetudo, D. Malz, P. Magnard, A. Akin, M. Gabureac, G. J. Norris, J. I. Cirac, A. Wallraff, and C. Eichler, *Nature Communications* **11**, 4877 (2020).

[17] D. C. McKay, S. Filipp, A. Mezzacapo, E. Magesan, J. M. Chow, and J. M. Gambetta, *Physical Review Applied* **6**, 10.1103/physrevapplied.6.064007 (2016).

[18] R. K. Naik, N. Leung, S. Chakram, P. Groszkowski, Y. Lu, N. Earnest, D. C. McKay, J. Koch, and D. I. Schuster, *Nature Communications* **8**, 10.1038/s41467-017-02046-6 (2017).

[19] J. D. Strand, M. Ware, F. Beaujardin, T. A. Ohki, B. R. Johnson, A. Blais, and B. L. T. Plourde, *Phys. Rev. B* **87**, 220505 (2013).

[20] E. A. Sete, N. Didier, A. Q. Chen, S. Kulshreshtha, R. Manenti, and S. Poletto, *Phys. Rev. Applied* **16**, 024050 (2021).

[21] M. Reagor, C. B. Osborn, N. Tezak, A. Staley, G. Prawiroatmodjo, M. Scheer, N. Alidoust, E. A. Sete, N. Didier, M. P. da Silva, and et al., *Science Advances* **4**, 10.1126/sciadv.aa03603 (2018).

[22] S. A. Caldwell, N. Didier, C. A. Ryan, E. A. Sete, A. Hudson, P. Karalekas, R. Manenti, M. P. da Silva, R. Sinclair, E. Acala, and et al., *Physical Review Applied* **10**, 10.1103/physrevapplied.10.034050 (2018).

[23] A. O. Niskanen, K. Harrabi, F. Yoshihara, Y. Nakamura, S. Lloyd, and J. S. Tsai, *Science* **316**, 723 (2007), <https://www.science.org/doi/pdf/10.1126/science.1141324>.

[24] J. Majer, J. M. Chow, J. M. Gambetta, J. Koch, B. R. Johnson, J. A. Schreier, L. Frunzio, D. I. Schuster, A. A. Houck, A. Wallraff, and et al., *Nature* **449**, 443–447 (2007).

[25] J. M. Chow, J. M. Gambetta, A. W. Cross, S. T. Merkel, C. Rigetti, and M. Steffen, *New Journal of Physics* **15**, 115012 (2013).

[26] J. Koch, T. M. Yu, J. Gambetta, A. A. Houck, D. I. Schuster, J. Majer, A. Blais, M. H. Devoret, S. M. Girvin, and R. J. Schoelkopf, *Phys. Rev. A* **76**, 042319 (2007).

[27] P. Krantz, M. Kjaergaard, F. Yan, T. P. Orlando, S. Gustavsson, and W. D. Oliver, *Applied Physics Reviews* **6**, 021318 (2019).

[28] P. Mundada, G. Zhang, T. Hazard, and A. Houck, *Phys. Rev. Applied* **12**, 054023 (2019), publisher: American Physical Society.

[29] A. Kandala, K. X. Wei, S. Srinivasan, E. Magesan, S. Carnevale, G. A. Keefe, D. Klaus, O. Dial, and D. C. McKay, arXiv:2011.07050 [quant-ph] (2020), arXiv: 2011.07050.

[30] F. Yan, S. Gustavsson, A. Kamal, J. Birenbaum, A. P. Sears, D. Hover, T. J. Gudmundsen, D. Rosenberg, G. Samach, S. Weber, and et al., *Nature Communications* **7**, 10.1038/ncomms12964 (2016).

[31] B. Kannan, A. Almanakly, Y. Sung, A. Di Paolo, D. A. Rower, J. Braumüller, A. Melville, B. M. Niedzielski, A. Karamlou, K. Serniak, A. Vepsäläinen, M. E. Schwartz, J. L. Yoder, R. Winik, J. I.-J. Wang, T. P. Orlando, S. Gustavsson, J. A. Grover, and W. D. Oliver, On-demand directional photon emission using waveguide quantum electrodynamics (2022).

[32] Z. Xiao, E. Doucet, T. Noh, L. Ranzani, R. W. Simmonds, L. C. G. Govia, and A. Kamal, Perturbative diagonalization for time-dependent strong interactions (2021), arXiv:2103.09260 [quant-ph].

[33] J. Braumüller, L. Ding, A. P. Vepsäläinen, Y. Sung, M. Kjaergaard, T. Menke, R. Winik, D. Kim, B. M. Niedzielski, A. Melville, and et al., *Physical Review Applied* **13**, 10.1103/physrevapplied.13.054079 (2020).

---

- [34] E. Kiktenko, A. Nikolaeva, P. Xu, G. Shlyapnikov, and A. Fedorov, *Physical Review A* **101**, 022304 (2020).
- [35] J. M. Baker, C. Duckering, and F. T. Chong, in *2020 IEEE 50th International Symposium on Multiple-Valued Logic (ISMVL)* (IEEE, 2020) pp. 303–308.
- [36] R.-P. Riwar and D. P. DiVincenzo, Circuit quantization with time-dependent magnetic fields for realistic geometries (2021), arXiv:2103.03577 [cond-mat.mes-hall].
- [37] U. Vool and M. Devoret, *International Journal of Circuit Theory and Applications* **45**, 897–934 (2017).
- [38] X. You, J. A. Sauls, and J. Koch, *Phys. Rev. B* **99**, 174512 (2019).
- [39] A. Altland and B. D. Simons, *Condensed Matter Field Theory*, 2nd ed. (Cambridge University Press, 2010).